Widefield *in vivo* imaging system with two fluorescence and two reflectance channels, a single sCMOS detector, and shielded illumination

Abbreviated title: Four-color mesoscope

Patrick R. Doran[1], Natalie Fomin-Thunemann[2], Rockwell P. Tang[1], Bernhard Zimmerman[2], Kıvılcım Kılıç[2], Emily A. Martin[2], Sreekanth Kura[2], Harrison P. Fisher[1], Grace Chabbott[3], Joel Herbert[4], John X. Jiang[2], Sava Sakadzic[5], David A. Boas[2], Anna Devor[2,5], Ichun Anderson Chen[2], Martin Thunemann[2]

[1]Graduate Program in Biomedical Engineering, Boston University, Boston, MA 02215, USA

[2]Department of Biomedical Engineering, Boston University, Boston, MA 02215, USA

[3]Undergraduate Program in Biomedical Engineering, Boston University, Boston, MA 02215, USA

[4]Undergraduate Program in Neuroscience, Boston University, Boston, MA 02215, USA

[5]Athinoula A. Martinos Center for Biomedical Imaging, Department of Radiology, Harvard Medical School, Massachusetts General Hospital, Charlestown, MA 02129, USA

Key words: mesoscope; mesoscale; cerebral cortex; fluorescence; hemoglobin absorption

[§]**Corresponding authors:**

Anna Devor and Martin Thunemann

610 Commonwealth Ave

Boston, MA 02215

USA

Email: adevor@bu.edu; martinth@bu.edu

Acknowledgements: We thank Ahmed Abdelfattah for generously providing purified mApple fluorescent protein for calibration of our imaging system. We gratefully acknowledge support from the NIH (BRAIN Initiative R01MH111359, BRAIN Initiative U19NS123717, R01DA050159, R01NS108472). Patrick Doran was supported by the Ruth L. Kirschstein Predoctoral Fellowship F31NS118949. Rockwell P. Tang was supported by NIGMS T32GM145455. The authors acknowledge that data analysis was performed on the Shared Computing Cluster which is administered by Boston University's Research Computing Services. We thank the members of the Neurovascular Imaging Laboratory for helpful discussions.

Author contributions: Patrick R. Doran: Investigation, Formal Analysis, Software, Visualization, Writing – original draft, Writing – review & editing; Natalie Fomin-Thunemann: Investigation, Writing – review & editing; Rockwell P. Tang: Investigation, Visualization, Writing – original draft, Writing – review & editing; Bernhard Zimmermann, Kıvılcım Kılıç, Joel D. Herbert, Grace Chabbott, John X. Jiang: Resources, Writing – review & editing; Sreekanth Kura, Harrison P. Fisher: Software, Writing – review & editing; Sava Sakadzic, David A. Boas: Conceptualization, Writing – review & editing; Anna Devor: Conceptualization, Funding acquisition, Supervision, Writing – original draft, Writing – review & editing; Ichun Anderson Chen: Conceptualization, Methodology, Supervision, Writing – review & editing; Martin Thunemann: Conceptualization, Software, Supervision, Visualization, Writing – original draft, Writing – review & editing.

Data availability: Design blueprints, parts inventory, data acquisition and analysis software, and data presented in this article are publicly available on github (https://github.com/NIL-NeuroScience/WidefieldImagingAnalysis).

Abstract

Significance: Widefield microscopy of the entire dorsal part of mouse cerebral cortex enables large-scale ("mesoscopic") imaging of neuronal activity with fluorescent indicators as well as hemodynamics via oxy- and deoxyhemoglobin absorption. Versatile and cost-effective imaging systems are needed for large-scale, color-multiplexed imaging of multiple fluorescent and intrinsic contrasts.

Aim: Develop a system for mesoscopic imaging of two fluorescent and two reflectance channels.

Approach: Excitation of red and green fluorescence is achieved through epi-illumination. Hemoglobin absorption imaging is achieved using 525- and 625-nm LEDs positioned around the objective lens. An aluminum hemisphere placed between objective and cranial window provides diffuse illumination of the brain. Signals are recorded sequentially by a single sCMOS detector.

Results: We demonstrate performance of our imaging system by recording large-scale spontaneous and stimulus-evoked neuronal, cholinergic, and hemodynamic activity in awake head-fixed mice with a curved "crystal skull" window expressing the red calcium indicator jRGECO1a and the green acetylcholine sensor $GRAB_{ACh3.0}$. Shielding of illumination light through the aluminum hemisphere enables concurrent recording of pupil diameter changes.

Conclusions: Our widefield microscope design with single camera can be used to acquire multiple aspects of brain physiology and is compatible with behavioral readouts of pupil diameter.

63 ## Introduction

64 With the rapidly expanding list of fluorescent probes for neuronal activity and the development of
65 large-scale measurements (Abdelfattah et al. 2022), widefield microscopy has become the
66 measurement modality of choice for mesoscale studies of neuronal circuits and underlying
67 behavior when cellular resolution is not required (Bouchard et al. 2009, Mohajerani et al. 2013,
68 Ma et al. 2016b, Vanni et al. 2017, Wright et al. 2017, Couto et al. 2021). Probes available in
69 distinct spectral variants (Zhao et al. 2011) can be spectrally multiplexed for simultaneous imaging
70 of different aspects of neuronal activity (Lin and Schnitzer 2016). Using multiplexed probes for in
71 vivo widefield imaging of head-fixed mice with “crystal skull” cranial windows (Kim et al. 2016)
72 provides a view of the entire dorsal part of the cerebral cortex including the primary sensory, motor
73 and higher association areas (Higley and Cardin 2022).

74 In the healthy brain, increases in neuronal activity are often accompanied by increases in blood
75 flow, volume, and oxygenation in the active region. The increase in blood flow and volume occurs,
76 in large part, due to dilation of cerebral arterioles responding to vasoactive messengers released
77 by active neurons (Uhlirova et al. 2016b, Echagarruga et al. 2020). This hemodynamic response
78 increases oxygen supply beyond the actual demand leading to a net increase in blood
79 oxygenation. Both oxy- and deoxyhemoglobin (HbO and HbR, respectively) strongly absorb light
80 in the blue-green spectrum. Therefore, the hemodynamic response results in time-variant
81 modulation of fluorescence signals within that spectral range. The methods developed to correct
82 fluorescent signals for this hemodynamic artifact fall into two categories. For the first correction
83 method, enhanced green fluorescent protein (EGFP)-based indicators, including GCaMP,
84 iGluSnFR, and GRAB indicators, are excited off-peak at their isosbestic point in the 390-420 nm
85 range (Lerner et al. 2015, Allen et al. 2017, Musall et al. 2019, Lake et al. 2020, Couto et al. 2021).
86 When excited at these wavelengths, fluorescence emission is independent from the analyte
87 concentration (i.e., [Ca^{2+}], [Glutamate], etc.), but affected by hemodynamic changes (Dana et al.

88 2019, Jing et al. 2020). This signal can then be regressed out of the analyte-dependent signal to
89 remove hemodynamic artifacts. Another correction method requires simultaneous acquisition of
90 light absorption of (at least two) wavelengths to quantify changes in HbO and HbR concentrations
91 (Δ[HbO] and Δ[HbR])(Ma et al. 2016b, Mitra et al. 2018). Furthermore, quantitative estimates of
92 Δ[HbO] and Δ[HbR] are important measurables on their own; they aid in understanding
93 cerebrovascular physiology and interpretation of non-invasive imaging signals generated through,
94 for example, functional magnetic resonance imaging (fMRI) (Uhlirova et al. 2016a).

95 Here, we describe a versatile widefield imaging system that enables two-color fluorescence
96 imaging in addition to concurrent acquisition of two absorption channels for quantitative estimation
97 of Δ[HbO] and Δ[HbR] with a single sCMOS detector. We shield the illumination light to prevent it
98 from reaching the animal's eyes using an aluminum light-blocking hemisphere to avoid unwanted
99 visual stimulation of the animal. Here, we provide optical design blueprints, a wiring diagram, a
100 timing chart, data acquisition software, and an inventory of all parts. We demonstrate the
101 performance of our new widefield microscope in awake mice expressing the mApple-based
102 calcium indicator jRGECO1a (Dana et al. 2016) and the EGFP-based acetylcholine (ACh) probe
103 $GRAB_{ACh3.0}$ (Jing et al. 2020).

Results

We designed and manufactured a widefield imaging system with a field of view of 10×10 mm^2 covering the dorsal cortex of a mouse. We use a single sCMOS detector for sequential recording of two fluorescent indicators (here: EGFP-derived $GRAB_{ACh3.0}$ and mApple-derived jRGECO1a) as well as hemoglobin absorption at 525 and 625 nm at an effective frame rate of 10 Hz or better without changes in the configuration of the emission path. **Figure 1** and **Supplementary Figure 1** provide an overview of the system layout and illustrate the spectral properties of the light sources and filter elements together with HbO and HbR absorption spectra as well as jRGECO1a and $GRAB_{ACh3.0}$ excitation and emission spectra. For fluorescence excitation, we use epi-illumination through the objective lens. A 470-nm LED with a maximal power of 3.7 W provides light for $GRAB_{ACh3.0}$ excitation, which is filtered through a 466/40 nm excitation bandpass filter, resulting in a maximal power of 403 mW at the sample surface. For jRGECO1a excitation, we use light from a 565-nm LED with a maximal power of 8.6 W which is filtered through a 560/14 nm excitation bandpass filter reaching a maximal power of 75 mW at the sample surface. A secondary peak in the 565-nm LED spectrum at ~425 nm is removed by an additional 450-nm longpass filter in the excitation path (**Figure 1A**). The collimated and filtered light is coupled into the infinity space using a multiband dichroic mirror (488/561 nm, 'main dichroic mirror'). This, in combination with a multi-band 'detection' filter (523/610 nm), allows $GRAB_{ACh3.0}$ and jRGECO1a fluorescence at 500-540 nm and 580-640 nm, respectively, to reach the sCMOS detector while blocking excitation light at 440-480 nm and 550-570 nm from reaching the camera (**Figure 1C-D**). Typical powers at the sample surface during image acquisition were 90-177 mW and 68-75 mW for 470 nm and 565 nm, respectively. We observed no or minimal bleaching over continuous acquisition periods of up to 30 minutes. The wavelengths for hemoglobin absorption imaging are within the respective emission bands of the green (525 nm) and red (625 nm) fluorophore (**Figure 1E**). The LEDs used for hemoglobin absorption imaging are placed in a custom-designed reflectance illumination ring

129 (RIR) located between the objective lens and the sample surface (**Figure 1B** and **Supplementary**
130 **Figure 1D**). The RIR contains six 525-nm LEDs and six 625-nm LEDs positioned at equal
131 distances with maximal powers of 170 mW and 371 mW per LED, respectively. To enable a
132 simple procedure for estimation of Δ[HbR] and Δ[HbO], we placed 10-nm bandpass filters in front
133 of each LED. This leads to a maximal power of 39.5 mW (525 nm) and 51 mW (625 nm) at the
134 sample surface. We placed a hollow aluminum hemisphere between the RIR and the sample
135 surface internally reflecting the light of the 525-nm and 625-nm LEDs. For imaging, the opening
136 of the hemisphere is brought close to the sample surface achieving diffuse and homogenous
137 illumination and efficiently eliminating most reflections from the curved glass window covering the
138 brain surface. Typical powers at the sample surface during image acquisition were 10.5 mW and
139 4.4 mW for the 525-nm and 625-nm LEDs, respectively.

140 To acquire all parts of the image simultaneously with a sCMOS camera with rolling shutter, we
141 ensure that the LEDs emit light only when all rows of the sCMOS chip are exposed. Therefore,
142 we control the LED drivers with two digital trigger signals combined through a logical AND gate
143 integrated circuit (IC) (**Figure 2**). The first input to the AND gate IC is generated by the camera
144 and is in 'high'-state when all rows are being exposed; the second input is generated by the
145 microscope control computer and selects the respective LED wavelength to be switched on
146 (**Figure 2**). Only when both signals are in 'high' state, the LED power supply receives a trigger
147 signal to switch the respective LED on. Timing delays of the AND gate IC and the LED driver are
148 <9 ns and <100 µs, respectively, enabling virtually delay-free LED power switches for typical
149 exposure times of 2-8 ms per individual LED.

150 The imaging setup is controlled through a DAQ interface programmed via MATLAB. The main
151 acquisition script generates digital trigger signals controlling the imaging setup based on exposure
152 time, which can be different for every wavelength, acquisition rate, and total acquisition time.
153 Additional triggers are generated to synchronize or control external devices such as stimulus

154 apparatuses, behavioral cameras, electrophysiology recording equipment, and behavioral control
155 devices. The currents of the individual LEDs are set in MATLAB and sent via a USB-based
156 remote-control interface to the LED drivers. The sCMOS camera is controlled through the
157 manufacturer's software where parameters such as field of view and on-camera pixel binning are
158 set. This software also drives image acquisition; however, the camera is set to respond to
159 exposure triggers generated by the DAQ interface, with the (variable) trigger length determining
160 the exposure time. During acquisition, the DAQ interface records feedback signals from camera,
161 microscope control, and external devices allowing synchronization of data streams during off-line
162 post-processing and analysis.

163 While our single-camera approach reduces complexity and cost, we use multiband filters to image
164 two fluorophores present in the sample at the same time. The lack of spectral separation on the
165 emission side can potentially create crosstalk when fluorophores are excited off-resonance. Note
166 that both fluorophores undergo dynamic changes in fluorescence intensity, so the degree of
167 crosstalk will vary in time and space. Published spectra show that $GRAB_{ACh3.0}$ (or EGFP) is
168 essentially not excited at 565 nm, while jRGECO1a (or mApple) fluorescence is excited at
169 470 nm. To quantify the amount of crosstalk under well-controlled conditions, we collected images
170 of purified EGFP and mApple proteins with various combinations of illumination power and
171 exposure time for both the 470-nm and 565-nm LEDs. In line with the published spectra, we
172 observed that the 565-nm LED practically does not excite purified EGFP while mApple shows
173 fluorescence when excited with the 470 nm LED (**Supplementary Figure 2A**). Based on this *in*
174 *vitro* calibration with EGFP and mApple and the typical acquisition parameters we used for *in vivo*
175 imaging in $GRAB_{ACh3.0}$ and jRGECO1a expressing animals, we determined that the level of
176 crosstalk of $GRAB_{ACh3.0}$ to fluorescence measured upon 565-nm excitation is <1%, while
177 fluorescence from jRGECO1a contributes about 3-9% to the fluorescence intensity measured
178 upon 470-nm excitation (**Supplementary Figure 2**; see **Appendix B** for a detailed discussion of

179 the crosstalk analysis). The in-vitro calibration allows to correct for crosstalk; however, given the
180 relatively small degree of crosstalk, we did not apply the correction term as it potentially adds
181 additional noise without sufficient benefit (see **Appendix B** for a detailed discussion).

182 To demonstrate the capabilities of our new imaging system design, we recorded spontaneous
183 and stimulus-induced changes in neuronal calcium, acetylcholine, and hemodynamic signals in
184 awake head-fixed mice expressing jRGECO1a and $GRAB_{ACh3.0}$ (**Figure 3**). Mice were implanted
185 with a curved glass cranial window exposing both hemispheres of the dorsal cortex while leaving
186 the bone in-between the two hemispheres above the superior sagittal sinus intact (Kilic et al.
187 2020) (**Figure 3A**). Images were registered to the Allen Mouse Common Coordinate Framework
188 (Wang et al. 2020) to generate time courses from pre-defined regions of the dorsal cortex.
189 Measurements of spontaneous activity show a high correlation between neuronal calcium and
190 ACh time courses (**Figure 3B** shows right secondary motor cortex), which is consistent with
191 published results (Lohani et al. 2022). We then recorded the response to a sensory stimulus
192 consisting of a 2-s, 3-Hz air puff sequence (20 repetitions, 25 s inter-stimulus interval) delivered
193 to the right whisker pad (**Figure 3C-E**). Ratio maps show neuronal activation and functional
194 hyperemia in the contralateral barrel cortex (green ROI in calcium map, **Figure 3C**). The stimulus-
195 averaged time course calculated from the contralateral barrel cortex shows that the imaging
196 system operates at sufficient signal to noise ratio to record the neuronal calcium response to the
197 six individual air puffs comprising one stimulus train (**Figure 3D**). Despite high trial-to-trial
198 variability (**Figure 3E**), which is consistent with published widefield imaging studies in awake mice
199 (Musall et al. 2019), responses to individual air puffs are still discernible in individual trial
200 recordings. The time course of the hemodynamic response shows a broad peak and post-stimulus
201 undershoot. The hemodynamic correction we apply to the green fluorophore compensates for
202 darkening that occurs when hemoglobin levels increase. **Supplementary Figure 3** compares the
203 trial averaged ACh time courses with and without correction for hemodynamic artifacts.

204 The aluminum hemisphere in-between the cranial window and the imaging system reflects 525-
205 and 625-nm light to improve the even distribution of illumination light for hemoglobin absorption
206 imaging. However, we observe some degree of inhomogeneity due to the curvature of glass
207 window (**Figure 3A**). At the same time, the hemisphere acts as a shield preventing the strobing
208 illumination light from reaching the mouse's eyes. For example, four-color imaging with an
209 effective acquisition rate of 10 Hz would produce an undesired visual stimulus at 40 Hz. To
210 illustrate the shielding effect, we recorded changes of the animal's pupil diameter during
211 mesoscopic imaging in presence or absence of the aluminum hemisphere (**Figure 4**). For this
212 experiment, a behavioral camera recorded the pupil diameter continuously while widefield
213 illumination across the four wavelengths at 40 Hz was switched on and off at 60-s intervals; we
214 recorded 20 off-to-on and on-to-off transitions per test. The images shown in **Figure 4A** show the
215 pupil before and after turning illumination on; **Supplementary Video 1** shows a recording of the
216 off-to-on transition with and without hemisphere. **Figure 4B** shows representative 2-min time
217 series covering the off-to-on and on-to-off transitions in presence or absence of the hemisphere.
218 Without the hemisphere, pupil size measurements are largely dominated by the state of widefield
219 illumination. In the presence of the hemisphere, pupil size changes are largely independent from
220 widefield illumination (**Figure 4C**). Then, we compared the relative change in pupil size from 1.5-
221 0.5 s before versus 2-3 s after start of widefield illumination averaged over 20 transitions and
222 observe a significantly larger drop in pupil size without the hemisphere ($p<0.001$; t-test; **Figure**
223 **4D**). Pupil tracking is often used as an important variable to define behavioral states (Vinck et al.
224 2015, Reimer et al. 2016) and it is therefore desirable to combine pupil recordings and mesoscale
225 imaging (Shahsavarani et al. 2023). In our system, the hemisphere eliminates interference of
226 widefield illumination on behavioral recordings and enables high-quality measurements of pupil
227 dynamics during mesoscale imaging.

228 ## Discussion

229 Here, we describe a new widefield microscope design for mesoscopic imaging of dorsal mouse
230 cortex. Several publications describe widefield calcium imaging with a single fluorescent indicator
231 and concurrent hemodynamic imaging (Bouchard et al. 2009, Ma et al. 2016b, Wright et al. 2017,
232 Mitra et al. 2018, Shahsavarani et al. 2023). Others describe two-color fluorescence widefield
233 imaging without hemodynamic imaging (Feng et al. 2019, Lohani et al. 2022). Compared to
234 previous publications, our system has several unique features:

235 First, the system enables quasi-simultaneous imaging of two spectrally distinct fluorophores
236 (here: EGFP-based $GRAB_{ACh3.0}$ and mApple-based jRGECO1a) together with quantitative
237 estimates of Δ[HbO] and Δ[HbR] through two-color absorption imaging. Changes in [HbO] and
238 [HbR] are used to correct hemodynamic artifacts of the recorded fluorescence signals. Further,
239 we can use them to study the relationship between cortical hemodynamics and different aspects
240 of brain activity, such as neuronal firing and neuromodulation thereby gaining further insights into
241 brain state-dependent regulation of cerebral blood flow and metabolism (Machler et al. 2021).

242 Second, we use a single detector. Using one camera drastically reduces the overall cost to build
243 the system but requires sequential image acquisition for every wavelength (here: four
244 wavelengths). We achieve sufficient SNR with negligible spectral crosstalk at a 10 Hz acquisition
245 rate, which is within the range for widefield imaging studies in awake animals (Lake et al. 2020,
246 Lohani et al. 2022).

247 Finally, the illumination light is contained within an aluminum hemisphere. Besides improving the
248 uniformity of illumination with the 525- and 625-nm LEDs, the hemisphere blocks most of the
249 illumination light from the animal's view, thereby preventing interference with behavioral
250 measurements of pupil diameter as well as unwanted stimulation of the visual system. Pupil size
251 measurements are often used as a non-invasive, indirect readout of alertness (Joshi et al. 2016,

252 Reimer et al. 2016). We expect our shielded illumination design will enable seamless integration
253 of mesoscale imaging with behavioral experiments based on visual stimulation (Vinck, Batista-
254 Brito et al. 2015, Peters, Fabre et al. 2021) and virtual reality (Pinto, Rajan et al. 2019).

255 The overall cost to build our widefield imaging system with the components used is around
256 $45,000, with the camera comprising the bulk of the cost (~$25000). While this is a lower price
257 than for typical commercially available widefield imaging systems, modifications could further
258 reduce the overall cost of the system. Depending on the brightness of the used fluorophores, their
259 expression level, as well as the experimental demands, it is possible that sufficient imaging
260 performance could be achieved with a less expensive camera. Furthermore, we used
261 commercially available LED drivers as well as commercially available LEDs for fluorescence
262 excitation. Using a custom design or already available open-source components with similar
263 performance characteristics, especially regarding their response time to digital triggers, could
264 further reduce the overall cost.

265 Our imaging system can easily be modified or expanded to suit the requirements of different
266 experimental studies; changing a LED and the corresponding optical filters will allow combining
267 other fluorescent indicators if they are spectrally separated. This would, for example, allow
268 integration of calcium indicators excited with near-infrared light (Qian et al. 2020). As the spectral
269 diversity of genetically encoded molecular probes expands, widefield imaging with three spectrally
270 separated fluorescent indicators might soon become a feasible approach. Furthermore, we and
271 others combined mesoscale imaging with extracellular electrophysiology, providing simultaneous
272 access to cortical network activity as well as single- or multi-unit activity in targeted cortical and
273 subcortical areas (Allen et al. 2017, Thunemann et al. 2018, Lu et al. 2023).

274 Our current system design has the following limitations. First, uneven illumination causes different
275 levels of absolute image brightness across the field of view. In practice, however, varying absolute

276 intensities will not affect the readout of relative (i.e., intensity-normalized) changes in fluorescence
277 or absorption, except for potentially reduced signal-to-noise levels in darker regions of the image.
278 A possible solution to overcome uneven illumination is the incorporation of an integration device
279 with uniformity correction, such as EUCLID (Celebi et al. 2023) into our imaging system. Further,
280 uneven illumination in the medial-to-lateral direction is also caused by the curvature of the glass
281 window covering the cranial exposure (see **Figure 3A**). Use of curved glass also causes different
282 cortical depths to match the focal plane of the imaging system, which potentially introduces
283 spatially heterogenous sampling bias. Here, use of adaptive lens optics, such as meta-lenses
284 (Yang et al. 2023) could improve uniformity of illumination and could be used to match the focal
285 plane across the field of view. Finally, in our experimental animals, we removed the dorsal cranium
286 and replaced it with a curved glass window. In some preparations for mesoscopic imaging, the
287 skull is thinned, polished, and covered with a glass coverslip, leaving the interface between brain
288 and bone intact (Silasi et al. 2016). While we do not expect performance or quality issues to arise
289 when imaging transcranial preparations with our setup, we consider a careful side-by-side
290 comparison of these two window preparations a valuable subject of future experiments. Designing
291 an imaging system with a single camera reduces overall system cost. However, the use of two
292 cameras would allow for higher acquisition rates through spectral multiplexing. Further, the dual-
293 band dichroic mirror and emission filter cut the available spectral bandwidth of the
294 EGFP/GRAB$_{ACh3.0}$ emission band (500-540 nm) and the mApple/jRGECO1a excitation band (550-
295 570 nm). This potentially enables crosstalk due to off-peak excitation of the red fluorophore.
296 However, we achieve sufficient SNR with negligible spectral crosstalk at a 10 Hz acquisition rate,
297 which is within the range of appropriate temporal resolution for widefield imaging studies in awake
298 animals (Lake, Ge et al. 2020, Lohani, Moberly et al. 2022). Furthermore, the extension of the
299 imaging system by a second camera requires minimal modifications to the overall layout, allowing
300 for higher acquisition speeds, if desired. Another consideration during the design of our system
301 was the use of lasers instead of LEDs for excitation of the green and red fluorescent proteins.

While less expensive, LEDs have a broad emission spectrum that requires clean-up through excitation filters. This limits the emitted light to the usable spectral range (see, e.g., **Figure 1D**, 565-nm LED) leading to an overall reduction in the available power compared to the nominal output (75 mW versus 8.6 W for the 565-nm LED), potentially requiring longer integration times to achieve sufficient SNRs. Here, use of a laser would enable excitation at higher power levels, if required. A drawback of using lasers instead of LEDs would be a substantial increase in the cost of the system.

In summary, given the versatility of our system and the comparatively low cost in contrast to commercial intravital imaging setups, we expect our widefield imaging system design to become a useful platform in the neuroscience and neurophotonics community.

312 # Methods

313 **Experimental animals**

314 All procedures were conducted with approval from Boston University Institutional Animal Care
315 and Use Committee and in accordance with the National Institutes of Health Guide for the Care
316 and Use of Laboratory Animals. Standard rodent chow and water were provided ad libitum. Mice
317 were housed in a 12-hour light cycle with lights turning on at 7:30 AM. We used three female mice
318 of the Thy1-jRGECO1a GP8.20 (Dana et al 2016, Dana et al 2019, Lin et al 2016) line; cortex-
319 wide $GRAB_{ACh3.0}$ expression was induced by injection of 1.5 μL AAV9-hSyn-$GRAB_{ACh3.0}$ (WZ
320 Biosciences, 3.06×10^{13} GC/mL) into each transverse sinus (3 μL per animal) of 1-day old
321 neonates according to procedures described in Lohani et al. (2022).

322 Headpost implantation and craniotomy in adult (8-16 week old) animals follows procedures
323 described in Kilic et al. (2020). Briefly, a custom-designed headpost machined from titanium was
324 attached to the cranium and a modified crystal skull curved glass window was used to replace the
325 dorsal cranium on both hemispheres (Kim et al. 2016). Prior to surgery, the original curved glass
326 (12 mm width, labmaker.org) was cut in half to obtain separate glass pieces for each hemisphere.
327 Following the implantation procedure, a silicone plug was placed on top of the glass window and
328 a 3D-printed cap was fixed to the headpost to prevent heat loss. Mice were allowed to recover for
329 at least one week following surgery before behavioral training commenced.
330 To adapt mice to be comfortable under head fixation, animals were handled until they remained
331 calm in the gloved hand of the investigator. Mice were then head-fixed for increasing periods while
332 they received a reward of sweetened condensed milk. Data acquisition was started when animals
333 tolerated one hour of head fixation.

334 **Imaging system optical components**

335 The imaging system is assembled from standard optomechanical components compatible with 2-

336 inch lens tubes. The imaging system is placed on an elevated platform (61×61 cm, Thorlabs,
337 MB2424) on a vibration-isolating table.
338 A 470-nm LED (Thorlabs, SOLIS-470C) is used to excite $GRAB_{ACh3.0}$ and a 565-nm LED
339 (Thorlabs, SOLIS-565C) is used to excite jRGECO1a. A 466/40 nm excitation filter (Semrock,
340 FF01-466/40, diameter 50 mm) is placed in front of the 470-nm LED and a 560/14 nm excitation
341 filter (Semrock, FF01-560/14, diameter 50 mm) is placed in front of the 565-nm LED. A dichroic
342 mirror combines excitation light from 565-nm and 470-nm LEDs (Semrock, FF520-Di02, 50 x 72
343 mm). The output of these LEDs is filtered through a 450-nm longpass filter (Chroma, AT450lp) to
344 remove low wavelength light from the 565 nm LED that leaks through the primary excitation filter.
345 A 45-degree mirror (Thorlabs, PF20-03-P01, diameter 50.8 mm) reflects excitation light down
346 towards the mouse and reflects emitted light into the plane of the camera. A dual-band 'main'
347 dichroic beam splitter (Semrock, Di03-R488/461, 50 x 72 mm) reflects excitation light towards the
348 mirror and transmits emitted light towards the camera. A dual-band emission filter (Semrock,
349 FF01-523/610, diameter 50 mm) is placed between a dichroic mirror and camera. A tube lens
350 (Olympus, MVX-TLU-MVX10) projects the image onto the sCMOS camera (Andor, Zyla 4.2P-
351 CL10 or Sona 4.2B-6).

352 An objective lens (Olympus, ZDM-1-MVX063) focuses the fluorescence excitation light onto the
353 brain for epi-illumination and projects the emitted light towards the camera. The objective lens is
354 surrounded by the reflective illumination ring (RIR) assembly, which contains six equally spaced
355 525 -nm LEDs (CREE LED, XBDGRN-00-0000-000000C02) and six equally spaced 625-nm
356 LEDs (CREE LED, XBDRED-00-0000-000000701) for reflectance imaging. Bandpass filters were
357 cut to 9.4-mm diameter and placed in front of the reflectance LEDs. These filters are 532/10 nm
358 bandpass filters (Edmund Optics, 65094) for the 525-nm LEDs and 632/10 nm bandpass filters
359 (Edmund Optics, 65105) for the 625-nm LEDs. Six Peltier elements (Ferro Tec, 81044) controlled
360 by a feedback-controlled temperature controller (Thorlabs, TED200C) actively cool the LEDs in

361 the RIR to maintain the LEDs at room temperature during data acquisition. Temperature is
362 measured on the LED ring with a 10-kΩ thermistor (TDK, NTCG163JF103FT1). Heat from the
363 Peltier elements is transferred to a custom heat sink made of aluminum. The RIR allows fixation
364 of custom hemisphere made of aluminum (bead-blasted) with a 15-mm opening located directly
365 above the cranial window.

366 **Control of imaging acquisition**

367 We use a computer-controlled DAQ device (National Instruments, PCIe-6363) to operate the
368 imaging system. The DAQ device is connected to two I/O connector boards (National Instruments,
369 CB-68LPR) inside a control interface box. The control interface relays a DAQ-generated exposure
370 trigger to the camera. An integrated circuit with an OR gate (Texas Instruments, SN74AHC32N)
371 within the control interface receives the “Fire ALL” trigger from the camera as an input. The “Fire
372 ALL” trigger is positive when all camera rows are exposed by the rolling shutter. The output of the
373 OR gate is the common input to an integrated circuit with four AND gates (Texas Instruments,
374 SN74AC08N). The second – wavelength-specific – input to each individual AND gate is the LED
375 selection trigger generated by the DAQ system. Each output of the AND gate connects to one
376 LED driver (Thorlabs, DC2200) controlling one type of LED. During normal operation of the
377 imaging system, the “Fire ALL” trigger controls when the LED turns on. The other input to the OR
378 gate is a camera bypass trigger that allows the LEDs to be triggered while the camera is off. We
379 use a custom MATLAB script to control the DAQ system. We used image capture software (Andor,
380 SOLIS) to control camera and image acquisition.

381 The animal was positioned under 525-nm illumination and the platform carrying the animal was
382 adjusted to bring the brain surface into focus. Then, the aluminum dome is lowered to minimize
383 the distance between its opening and the brain surface. Illumination intensities (i.e., LED currents)
384 were adjusted to bring image intensities into the dynamic range of the camera at 16-bit image
385 depth. The acquisition window was cropped to the size of the field of view; image height (number

386 of rows) was a variable entered into the MATLAB script controlling image acquisition: the length
387 of the period when all rows are exposed ("FIRE all") depends on image height and requires
388 adjustment of the camera exposure trigger generated by the DAQ system. Typical image sizes
389 were 460×360 pixels with a 9.2x7.2 mm field of view and 20 μm resolution at 4×4 binning. Based
390 on selected exposure times and frame rate, the MATLAB script calculates the total number of
391 frames per acquisition run; this number is entered into the image capture software. The camera
392 is set to "External Exposure" mode and image acquisition is started. Then, execution of the
393 MATLAB script is started causing the DAQ interface to send LED selection and camera triggers
394 to the control interface.

395 **Sensory stimulation and behavioral recordings**

396 The MATLAB acquisition script generates additional triggers for synchronization with behavioral
397 apparatuses, such as to deliver stimuli by puffing compressed air to the animals' whiskers. Stimuli
398 are defined by duration, frequency, repetitions, interstimulus interval for individual stimuli and
399 sequences of pre-stimulus baseline, stimulus, and post-stimulus observation period. Based on
400 these parameters, the MATLAB script calculates the required imaging time and number of
401 images. For air puff stimuli, the 5-V trigger is sent to a picopump (WPI, PV830) connected to a
402 2 -mm diameter plastic tube that terminates in a glass capillary to deliver pressurized air to the
403 mouse whiskers.

404 The animal's face and whiskers are recorded during imaging with a CCD camera (Basler,
405 acA1920-150uc) through a variable zoom lens (Edmund Optics, 67715). A 940-nm LED
406 (Thorlabs, M940L3) continuously illuminates the animal, and a 920-nm long pass filter prevents
407 light from the microscope from contaminating the camera recording. The mesoscope control
408 system triggers the CCD camera to acquire a single frame during each acquisition cycle.

409 An accelerometer (Analog Devices, ADXL335) is placed underneath the mouse bed to record
410 animal's motion. The accelerometer generates analog signals for motion in X, Y and Z direction

411 which are recorded by a separate DAQ system (NI, USB-6363) receiving a synchronization signal
412 from the mesoscope control system.

413 **Image processing**

414 The camera control software (Solis, Andor) stores the acquired images as raw data ('.dat')
415 together with metadata files ('.ini' and '.sifx'). For all subsequent import and processing steps, we
416 use MATLAB. Raw image data is loaded into MATLAB, bypassing conversion into image (.tif) files
417 by the camera software and enabling multi-stream data import from high-performance solid-state
418 drives with MATLAB's multi-processor environment. For all channels, a baseline image
419 representing the temporal average of all images for that channel is generated. For fluorescence
420 channels, ΔF/F images are computed on a pixel-by-pixel basis by dividing each image by the
421 baseline image. After calculating ΔF/F, linear trends are removed from the time course of each
422 pixel using the MATLAB function "detrend". The modified Beer-Lambert law is used to calculate
423 changes in HbO and HbR concentrations from 525 nm and 625 nm reflectance (see
424 implementation for MATLAB's multi-processor environment in Appendix A). Estimated Δ[HbO]
425 and Δ [HbR] are used to correct green fluorescence measurements for artificial intensity changes
426 caused by dynamic changes in excitation and emission light absorption by hemoglobin. The
427 correction method has been described in Ma et al. (2016a) and its implementation is further
428 detailed in **Appendix A**. In this correction approach, the measured fluorescence is equal to the
429 artifact-free change in fluorescence multiplied by a correction factor containing the pathlength of
430 in tissue and the tissue absorption coefficient. Pathlengths have been previously estimated based
431 on Monte Carlo simulations (Ma et al 2016). Since hemoglobin accounts for most of the light
432 absorption in brain tissue, light absorption depends largely on Δ[HbO] and Δ[HbR] and the known
433 HbO and HbR extinction coefficients at the respective wavelengths of fluorescence excitation and
434 emission. We calculate the light absorption coefficient for every pixel at every time point based

435 on our estimations of Δ[HbO] and Δ[HbR] and apply it to correct for hemodynamic darkening of
436 ΔF/F in the green (EGFP/$GRAB_{ACh3.0}$) channel.

437 Measurements with several consecutive trials are interpolated at 100-ms intervals using a time
438 vector relative to the stimulus onset. Trial-averaged ratio maps are calculated by averaging
439 individual time courses across trials.

440 Behavioral video recordings are stored as image sequences and imported into MATLAB. To
441 calculate pupil size, an elliptical region is drawn defining the eye and an intensity threshold is
442 manually defined. The pupil size is calculated as the number of pixels below the threshold. The
443 resulting time series is normalized to its maximal and minimal pupil size within the recording.

444 ***In Vitro* Crosstalk calibration**

445 Solutions of purified 0.03 mg/mL EGFP (Abcam, ab84191) and 0.4 mg/mL mApple (kindly
446 provided by Ahmed Abdelfattah) in phosphate-buffered saline (PBS) were prepared prior to
447 imaging. 30-μL samples of EGFP, mApple, or PBS-only control solution were each injected into
448 one channel of separate 6-channel slides (ibidi, μ-Slide VI – Flat). The center of the fluorophore-
449 filled channel was focused under the widefield imaging system before starting image acquisition
450 for each slide. Illumination during an imaging sequence alternated between the 470-nm and
451 565-nm LEDs while stepping through a series of camera exposure times and increasing LED
452 currents. Three trials were conducted for each sample, with the position of the slide under the
453 objective being shifted between trials to account for intensity variations. To calculate the
454 fluorescence intensity, pixel values were averaged over a region of interest covering the center
455 of the fluorophore-containing channel. Then, we took the mean of the three trials per condition
456 and subtracted the fluorescence intensity of the PBS control. Further analysis of crosstalk is
457 detailed in **Appendix B**.

458 ## Figure Legends

459 **Figure 1. Schematics of the wide field imaging system and fluorescence and reflectance**
460 **spectra. A.** A single sCMOS camera is used to measure emission of green and red fluorophores
461 and two hemoglobin absorption wavelengths. A 565-nm LED excites mApple-based jRGECO1a
462 and a 470-nm LED excites EGFP-based $GRAB_{ACh3.0}$; both LEDs are filtered through excitation
463 filters. The main dichroic mirror reflects excitation light towards a 45°-mirror and then a 0.63×
464 objective lens to focus the excitation light onto the sample. Below the objective lens is the
465 reflectance illumination ring (RIR) further detailed in panel B. An aluminum hemisphere between
466 the RIR and the sample surface internally reflects the 525- and 625-nm LEDs for homogenous
467 illumination and prevents illumination light from reaching the animal's eyes. Fluorescence
468 emission and reflectance pass the main dichroic and the detection filter before being focused by
469 a tube lens to the camera. **B.** Cross-section of the reflectance illumination ring (RIR) setup. Each
470 of the six 525- and 625-nm LEDs are arranged on a ring-shaped board at equal distances. Peltier
471 elements actively cool the LEDs to prevent temperature changes resulting in unstable illumination
472 intensities. 10 nm wide excitation filters are mounted in front of each LED. **C.** Excitation (solid blue
473 line) and emission (solid green line) of EGFP-derived $GRAB_{ACh3.0}$ (Jing et al. 2020). The light-blue
474 and dark-blue shaded areas represent the 470-nm LED spectrum before and after passing the
475 excitation filter (BP466/40, blue dotted line). **D.** Excitation (solid yellow line) and emission (solid
476 red line) spectrum of mApple-derived jRGECO1a (Dana et al. 2016). The light-orange and dark-
477 orange areas represent the 565-nm LED spectrum before and after passing the excitation filter
478 (BP560/14, orange dotted line). **E.** Absorption spectra of oxyhemoglobin (HbO, red line) and
479 deoxyhemoglobin (HbR, blue line) from Prahl (1999). LED spectra are confined by excitation
480 filters (525 nm in light and dark green; 625 nm in light and dark red before and after passing
481 through the respective excitation filters).

482 **Figure 2. Timing diagram to trigger LEDs and camera acquisition.** MATLAB controls the DAQ
483 system via digital triggers controlling camera and LED drivers. A different LED illuminates the
484 sample during each frame for near-simultaneous acquisition. The effective frame rate is
485 determined by the length of the four-frame cycle (typically 100 ms). Grey lines next to the camera
486 Fire ALL trigger represent exposure of pixel rows in rolling shutter mode. The Fire ALL trigger is
487 sent when all rows are exposed. Each LED driver (bottom left) is controlled by the output of a
488 separate AND gate. The Fire ALL trigger is the common input to every AND gate while the
489 individual LED selection triggers are the second input for each AND gate.

490 **Figure 3: Spontaneous and stimulus-evoked activity in the somatosensory cortex. A.**
491 Average of the first ten images collected during a ten-minute acquisition for each illumination
492 wavelength. The two hemispheres were manually masked around the cranial window. A green
493 polygon was drawn around the right secondary motor cortex, which was determined by
494 registration to the Allen atlas of the mouse brain. **B.** Spontaneous activity in the right secondary
495 motor cortex (green polygon in panel A) for calcium, acetylcholine (ACh), and oxygenated,
496 deoxygenated, and total hemoglobin (HbO, HbR, HbT). **C.** Ratio maps averaged across 20 trials
497 showing the response to a 2-s, 3-Hz train of air puffs to the right whisker pad. Maps show data
498 from 1.7 s after stimulus onset except for the calcium map, which shows data from 0.1 s after
499 stimulus onset. **D.** Average time course of the stimulus-evoked response in the contralateral barrel
500 cortex (green region in panel C). The pink dashed line indicates when the calcium ratio map in
501 panel C is shown whereas the black dashed line indicates when ACh, HbT and HbO ratio maps
502 in panel C are shown. The grey-shaded area indicates the duration of the stimulus. **E.** Response
503 of the contralateral barrel cortex to individual stimulus trains. The trials are sorted according to
504 the magnitude of the calcium response.

505 **Figure 4: The aluminum hemisphere shields illumination and reduces pupil constriction**
506 **during mesoscale imaging. A.** Images of the mouse face 0.5 s before and 5 s after widefield

imaging acquisition begins. Green circles highlight the pupils. **B.** Example two-minute pupil diameter time courses showing the off-to-on and on-to-off transition. The grey-shaded area indicates the period when widefield acquisition was performed **C.** Average pupil diameter changes upon beginning of widefield imaging (20 trials; traces show average ± standard deviation). Pupil diameter 1.5-0.5 s before imaging was defined as baseline for each trial. The green-dashed line indicates the start of widefield imaging, the black dashed lines indicate time points of the images shown in panel A. **D.** Comparison of the ratio of pupil size 2-3 s after start of imaging to pupil size 1.5-0.5 s before imaging. Significance was tested with a student's t test.

References

Abdelfattah, A. S., S. Ahuja, T. Akkin, S. R. Allu, J. Brake, D. A. Boas, E. M. Buckley, R. E. Campbell, A. I. Chen, X. Cheng, T. Cizmar, I. Costantini, M. De Vittorio, A. Devor, P. R. Doran, M. El Khatib, V. Emiliani, N. Fomin-Thunemann, Y. Fainman, T. Fernandez-Alfonso, C. G. L. Ferri, A. Gilad, X. Han, A. Harris, E. M. C. Hillman, U. Hochgeschwender, M. G. Holt, N. Ji, K. Kilic, E. M. R. Lake, L. Li, T. Li, P. Machler, E. W. Miller, R. C. Mesquita, K. Nadella, U. V. Nagerl, Y. Nasu, A. Nimmerjahn, P. Ondrackova, F. S. Pavone, C. Perez Campos, D. S. Peterka, F. Pisano, F. Pisanello, F. Puppo, B. L. Sabatini, S. Sadegh, S. Sakadzic, S. Shoham, S. N. Shroff, R. A. Silver, R. R. Sims, S. L. Smith, V. J. Srinivasan, M. Thunemann, L. Tian, L. Tian, T. Troxler, A. Valera, A. Vaziri, S. A. Vinogradov, F. Vitale, L. V. Wang, H. Uhlirova, C. Xu, C. Yang, M. H. Yang, G. Yellen, O. Yizhar and Y. Zhao (2022). "Neurophotonic tools for microscopic measurements and manipulation: status report." Neurophotonics **9**(Suppl 1): 013001.

Allen, W. E., I. V. Kauvar, M. Z. Chen, E. B. Richman, S. J. Yang, K. Chan, V. Gradinaru, B. E. Deverman, L. Luo and K. Deisseroth (2017). "Global Representations of Goal-Directed Behavior in Distinct Cell Types of Mouse Neocortex." Neuron **94**(4): 891-907 e896.

Bouchard, M. B., B. R. Chen, S. A. Burgess and E. M. Hillman (2009). "Ultra-fast multispectral optical imaging of cortical oxygenation, blood flow, and intracellular calcium dynamics." Opt Express **17**(18): 15670-15678.

Celebi, I., M. Aslan and M. S. Unlu (2023). "A spatially uniform illumination source for widefield multi-spectral optical microscopy." PLoS One **18**(10): e0286988.

Couto, J., S. Musall, X. R. Sun, A. Khanal, S. Gluf, S. Saxena, I. Kinsella, T. Abe, J. P. Cunningham, L. Paninski and A. K. Churchland (2021). "Chronic, cortex-wide imaging of specific cell populations during behavior." Nat Protoc **16**(7): 3241-3263.

Dana, H., B. Mohar, Y. Sun, S. Narayan, A. Gordus, J. P. Hasseman, G. Tsegaye, G. T. Holt, A. Hu, D. Walpita, R. Patel, J. J. Macklin, C. I. Bargmann, M. B. Ahrens, E. R. Schreiter, V. Jayaraman, L. L. Looger, K. Svoboda and D. S. Kim (2016). "Sensitive red protein calcium indicators for imaging neural activity." Elife **5**.

Dana, H., Y. Sun, B. Mohar, B. K. Hulse, A. M. Kerlin, J. P. Hasseman, G. Tsegaye, A. Tsang, A. Wong, R. Patel, J. J. Macklin, Y. Chen, A. Konnerth, V. Jayaraman, L. L. Looger, E. R. Schreiter, K. Svoboda and D. S. Kim (2019). "High-performance calcium sensors for imaging activity in neuronal populations and microcompartments." Nat Methods **16**(7): 649-657.

Echagarruga, C. T., K. W. Gheres, J. N. Norwood and P. J. Drew (2020). "nNOS-expressing interneurons control basal and behaviorally evoked arterial dilation in somatosensory cortex of mice." Elife **9**.

Feng, J., C. Zhang, J. E. Lischinsky, M. Jing, J. Zhou, H. Wang, Y. Zhang, A. Dong, Z. Wu, H. Wu, W. Chen, P. Zhang, J. Zou, S. A. Hires, J. J. Zhu, G. Cui, D. Lin, J. Du and Y. Li (2019). "A

Genetically Encoded Fluorescent Sensor for Rapid and Specific In Vivo Detection of Norepinephrine." Neuron **102**(4): 745-761 e748.

Higley, M. J. and J. A. Cardin (2022). "Spatiotemporal dynamics in large-scale cortical networks." Curr Opin Neurobiol **77**: 102627.

Jing, M., Y. Li, J. Zeng, P. Huang, M. Skirzewski, O. Kljakic, W. Peng, T. Qian, K. Tan, J. Zou, S. Trinh, R. Wu, S. Zhang, S. Pan, S. A. Hires, M. Xu, H. Li, L. M. Saksida, V. F. Prado, T. J. Bussey, M. A. M. Prado, L. Chen, H. Cheng and Y. Li (2020). "An optimized acetylcholine sensor for monitoring in vivo cholinergic activity." Nat Methods **17**(11): 1139-1146.

Joshi, S., Y. Li, R. M. Kalwani and J. I. Gold (2016). "Relationships between Pupil Diameter and Neuronal Activity in the Locus Coeruleus, Colliculi, and Cingulate Cortex." Neuron **89**(1): 221-234.

Kilic, K., M. Desjardins, J. Tang, M. Thunemann, S. Sunil, S. E. Erdener, D. D. Postnov, D. A. Boas and A. Devor (2020). "Chronic Cranial Windows for Long Term Multimodal Neurovascular Imaging in Mice." Front Physiol **11**: 612678.

Kim, T. H., Y. Zhang, J. Lecoq, J. C. Jung, J. Li, H. Zeng, C. M. Niell and M. J. Schnitzer (2016). "Long-Term Optical Access to an Estimated One Million Neurons in the Live Mouse Cortex." Cell Rep **17**(12): 3385-3394.

Lake, E. M. R., X. Ge, X. Shen, P. Herman, F. Hyder, J. A. Cardin, M. J. Higley, D. Scheinost, X. Papademetris, M. C. Crair and R. T. Constable (2020). "Simultaneous cortex-wide fluorescence Ca(2+) imaging and whole-brain fMRI." Nat Methods **17**(12): 1262-1271.

Lerner, T. N., C. Shilyansky, T. J. Davidson, K. E. Evans, K. T. Beier, K. A. Zalocusky, A. K. Crow, R. C. Malenka, L. Luo, R. Tomer and K. Deisseroth (2015). "Intact-Brain Analyses Reveal Distinct Information Carried by SNc Dopamine Subcircuits." Cell **162**(3): 635-647.

Lin, M. Z. and M. J. Schnitzer (2016). "Genetically encoded indicators of neuronal activity." Nat Neurosci **19**(9): 1142-1153.

Lohani, S., A. H. Moberly, H. Benisty, B. Landa, M. Jing, Y. Li, M. J. Higley and J. A. Cardin (2022). "Spatiotemporally heterogeneous coordination of cholinergic and neocortical activity." Nat Neurosci **25**(12): 1706-1713.

Lu, X., Y. Wang, Z. Liu, Y. Gou, D. Jaeger and F. St-Pierre (2023). "Widefield imaging of rapid pan-cortical voltage dynamics with an indicator evolved for one-photon microscopy." Nature Communications **14**(1): 6423.

Ma, Y., M. A. Shaik, S. H. Kim, M. G. Kozberg, D. N. Thibodeaux, H. T. Zhao, H. Yu and E. M. Hillman (2016a). "Wide-field optical mapping of neural activity and brain haemodynamics: considerations and novel approaches." Philos Trans R Soc Lond B Biol Sci **371**(1705): 20150360.

585 Ma, Y., M. A. Shaik, M. G. Kozberg, S. H. Kim, J. P. Portes, D. Timerman and E. M. Hillman
586 (2016b). "Resting-state hemodynamics are spatiotemporally coupled to synchronized and
587 symmetric neural activity in excitatory neurons." Proc Natl Acad Sci U S A **113**(52): E8463-E8471.

588 Machler, P., T. Broggini, C. Mateo, M. Thunemann, N. Fomin-Thunemann, P. R. Doran, I. Sencan,
589 K. Kilic, M. Desjardins, H. Uhlirova, M. A. Yaseen, D. A. Boas, A. A. Linninger, M. Vergassola, X.
590 Yu, L. D. Lewis, J. R. Polimeni, B. R. Rosen, S. Sakadzic, R. B. Buxton, M. Lauritzen, D. Kleinfeld
591 and A. Devor (2021). "A Suite of Neurophotonic Tools to Underpin the Contribution of Internal
592 Brain States in fMRI." Curr Opin Biomed Eng **18**: 100273.

593 Mitra, A., A. Kraft, P. Wright, B. Acland, A. Z. Snyder, Z. Rosenthal, L. Czerniewski, A. Bauer, L.
594 Snyder, J. Culver, J. M. Lee and M. E. Raichle (2018). "Spontaneous Infra-slow Brain Activity Has
595 Unique Spatiotemporal Dynamics and Laminar Structure." Neuron **98**(2): 297-305 e296.

596 Mohajerani, M. H., A. W. Chan, M. Mohsenvand, J. LeDue, R. Liu, D. A. McVea, J. D. Boyd, Y.
597 T. Wang, M. Reimers and T. H. Murphy (2013). "Spontaneous cortical activity alternates between
598 motifs defined by regional axonal projections." Nat Neurosci **16**(10): 1426-1435.

599 Musall, S., M. T. Kaufman, A. L. Juavinett, S. Gluf and A. K. Churchland (2019). "Single-trial
600 neural dynamics are dominated by richly varied movements." Nat Neurosci **22**(10): 1677-1686.

601 Prahl, S. (1999). "Optical Absorption of Hemoglobin." Retrieved 11/3/2023, 2023, from
602 https://omlc.org/spectra/hemoglobin/.

603 Qian, Y., D. M. O. Cosio, K. D. Piatkevich, S. Aufmkolk, W. C. Su, O. T. Celiker, A. Schohl, M. H.
604 Murdock, A. Aggarwal, Y. F. Chang, P. W. Wiseman, E. S. Ruthazer, E. S. Boyden and R. E.
605 Campbell (2020). "Improved genetically encoded near-infrared fluorescent calcium ion indicators
606 for in vivo imaging." PLoS Biol **18**(11): e3000965.

607 Reimer, J., M. J. McGinley, Y. Liu, C. Rodenkirch, Q. Wang, D. A. McCormick and A. S. Tolias
608 (2016). "Pupil fluctuations track rapid changes in adrenergic and cholinergic activity in cortex."
609 Nat Commun **7**: 13289.

610 Shahsavarani, S., D. N. Thibodeaux, W. Xu, S. H. Kim, F. Lodgher, C. Nwokeabia, M. Cambareri,
611 A. J. Yagielski, H. T. Zhao, D. A. Handwerker, J. Gonzalez-Castillo, P. A. Bandettini and E. M. C.
612 Hillman (2023). "Cortex-wide neural dynamics predict behavioral states and provide a neural
613 basis for resting-state dynamic functional connectivity." Cell Rep **42**(6): 112527.

614 Silasi, G., D. Xiao, M. P. Vanni, A. C. Chen and T. H. Murphy (2016). "Intact skull chronic windows
615 for mesoscopic wide-field imaging in awake mice." J Neurosci Methods **267**: 141-149.

616 Thunemann, M., Y. Lu, X. Liu, K. Kilic, M. Desjardins, M. Vandenberghe, S. Sadegh, P. A. Saisan,
617 Q. Cheng, K. L. Weldy, H. Lyu, S. Djurovic, O. A. Andreassen, A. M. Dale, A. Devor and D. Kuzum
618 (2018). "Deep 2-photon imaging and artifact-free optogenetics through transparent graphene
619 microelectrode arrays." Nat Commun **9**(1): 2035.

Uhlirova, H., K. Kilic, P. Tian, S. Sakadzic, L. Gagnon, M. Thunemann, M. Desjardins, P. A. Saisan, K. Nizar, M. A. Yaseen, D. J. Hagler, Jr., M. Vandenberghe, S. Djurovic, O. A. Andreassen, G. A. Silva, E. Masliah, D. Kleinfeld, S. Vinogradov, R. B. Buxton, G. T. Einevoll, D. A. Boas, A. M. Dale and A. Devor (2016a). "The roadmap for estimation of cell-type-specific neuronal activity from non-invasive measurements." Philos Trans R Soc Lond B Biol Sci **371**(1705).

Uhlirova, H., K. Kilic, P. Tian, M. Thunemann, M. Desjardins, P. A. Saisan, S. Sakadzic, T. V. Ness, C. Mateo, Q. Cheng, K. L. Weldy, F. Razoux, M. Vandenberghe, J. A. Cremonesi, C. G. Ferri, K. Nizar, V. B. Sridhar, T. C. Steed, M. Abashin, Y. Fainman, E. Masliah, S. Djurovic, O. A. Andreassen, G. A. Silva, D. A. Boas, D. Kleinfeld, R. B. Buxton, G. T. Einevoll, A. M. Dale and A. Devor (2016b). "Cell type specificity of neurovascular coupling in cerebral cortex." Elife **5**.

Vanni, M. P., A. W. Chan, M. Balbi, G. Silasi and T. H. Murphy (2017). "Mesoscale Mapping of Mouse Cortex Reveals Frequency-Dependent Cycling between Distinct Macroscale Functional Modules." J Neurosci **37**(31): 7513-7533.

Vinck, M., R. Batista-Brito, U. Knoblich and J. A. Cardin (2015). "Arousal and locomotion make distinct contributions to cortical activity patterns and visual encoding." Neuron **86**(3): 740-754.

Wang, Q., S. L. Ding, Y. Li, J. Royall, D. Feng, P. Lesnar, N. Graddis, M. Naeemi, B. Facer, A. Ho, T. Dolbeare, B. Blanchard, N. Dee, W. Wakeman, K. E. Hirokawa, A. Szafer, S. M. Sunkin, S. W. Oh, A. Bernard, J. W. Phillips, M. Hawrylycz, C. Koch, H. Zeng, J. A. Harris and L. Ng (2020). "The Allen Mouse Brain Common Coordinate Framework: A 3D Reference Atlas." Cell **181**(4): 936-953 e920.

Wright, P. W., L. M. Brier, A. Q. Bauer, G. A. Baxter, A. W. Kraft, M. D. Reisman, A. R. Bice, A. Z. Snyder, J. M. Lee and J. P. Culver (2017). "Functional connectivity structure of cortical calcium dynamics in anesthetized and awake mice." PLoS One **12**(10): e0185759.

Yang, F., M. Y. Shalaginov, H.-I. Lin, S. An, A. Agarwal, H. Zhang, C. Rivero-Baleine, T. Gu and J. Hu (2023). "Wide field-of-view metalens: a tutorial." Advanced Photonics **5**(03): 033001.

Zhao, Y., S. Araki, J. Wu, T. Teramoto, Y. F. Chang, M. Nakano, A. S. Abdelfattah, M. Fujiwara, T. Ishihara, T. Nagai and R. E. Campbell (2011). "An expanded palette of genetically encoded Ca(2)(+) indicators." Science **333**(6051): 1888-1891.

Figure 1

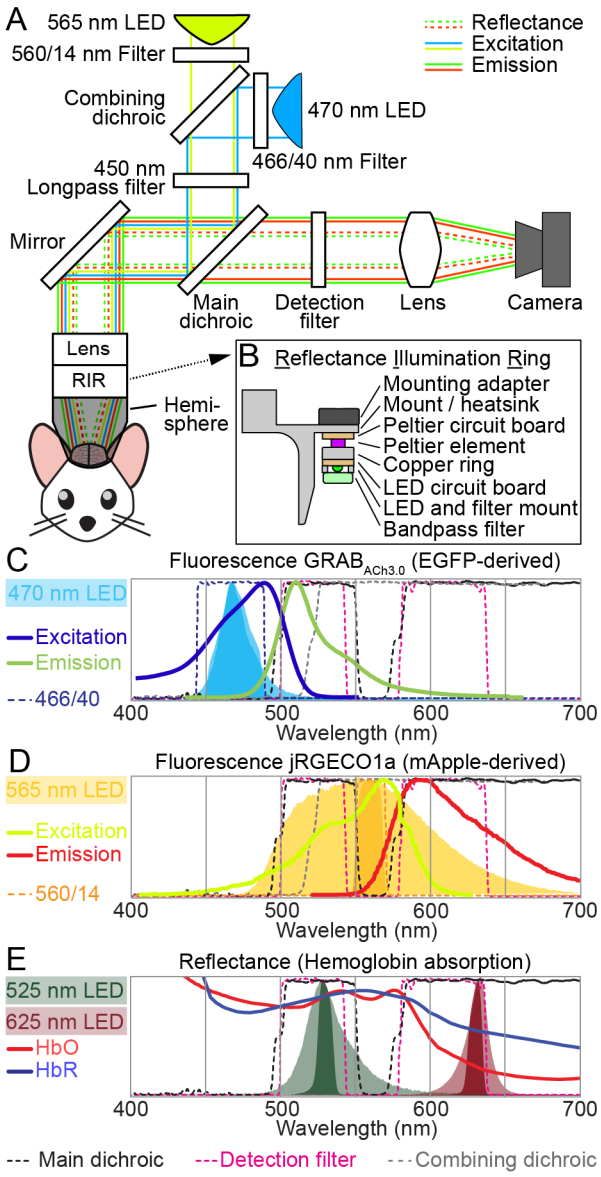
A
565 nm LED
560/14 nm Filter
Combining dichroic
470 nm LED
466/40 nm Filter
450 nm Longpass filter
Mirror
Main dichroic
Detection filter
Lens
Camera
Reflectance
Excitation
Emission
Lens
RIR
Hemi-sphere
B Reflectance Illumination Ring
Mounting adapter
Mount / heatsink
Peltier circuit board
Peltier element
Copper ring
LED circuit board
LED and filter mount
Bandpass filter
C
Fluorescence GRAB$_{ACh3.0}$ (EGFP-derived)
470 nm LED
Excitation
Emission
466/40
400
500
600
700
Wavelength (nm)
D
Fluorescence jRGECO1a (mApple-derived)
565 nm LED
Excitation
Emission
560/14
400
500
600
700
Wavelength (nm)
E
Reflectance (Hemoglobin absorption)
525 nm LED
625 nm LED
HbO
HbR
400
500
600
700
Wavelength (nm)
Main dichroic
Detection filter
Combining dichroic

Figure 2

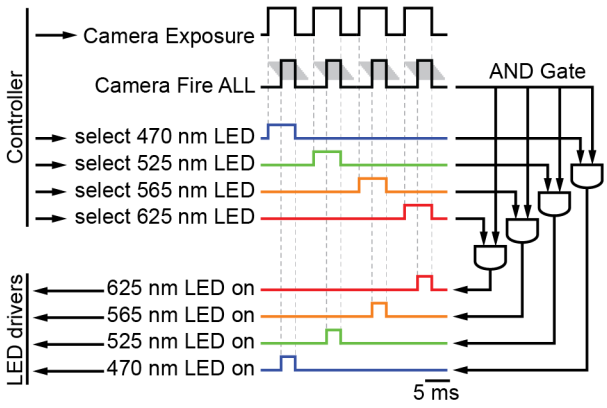
Controller
Camera Exposure
Camera Fire ALL
AND Gate
select 470 nm LED
select 525 nm LED
select 565 nm LED
select 625 nm LED
LED drivers
625 nm LED on
565 nm LED on
525 nm LED on
470 nm LED on
5 ms

Figure 3

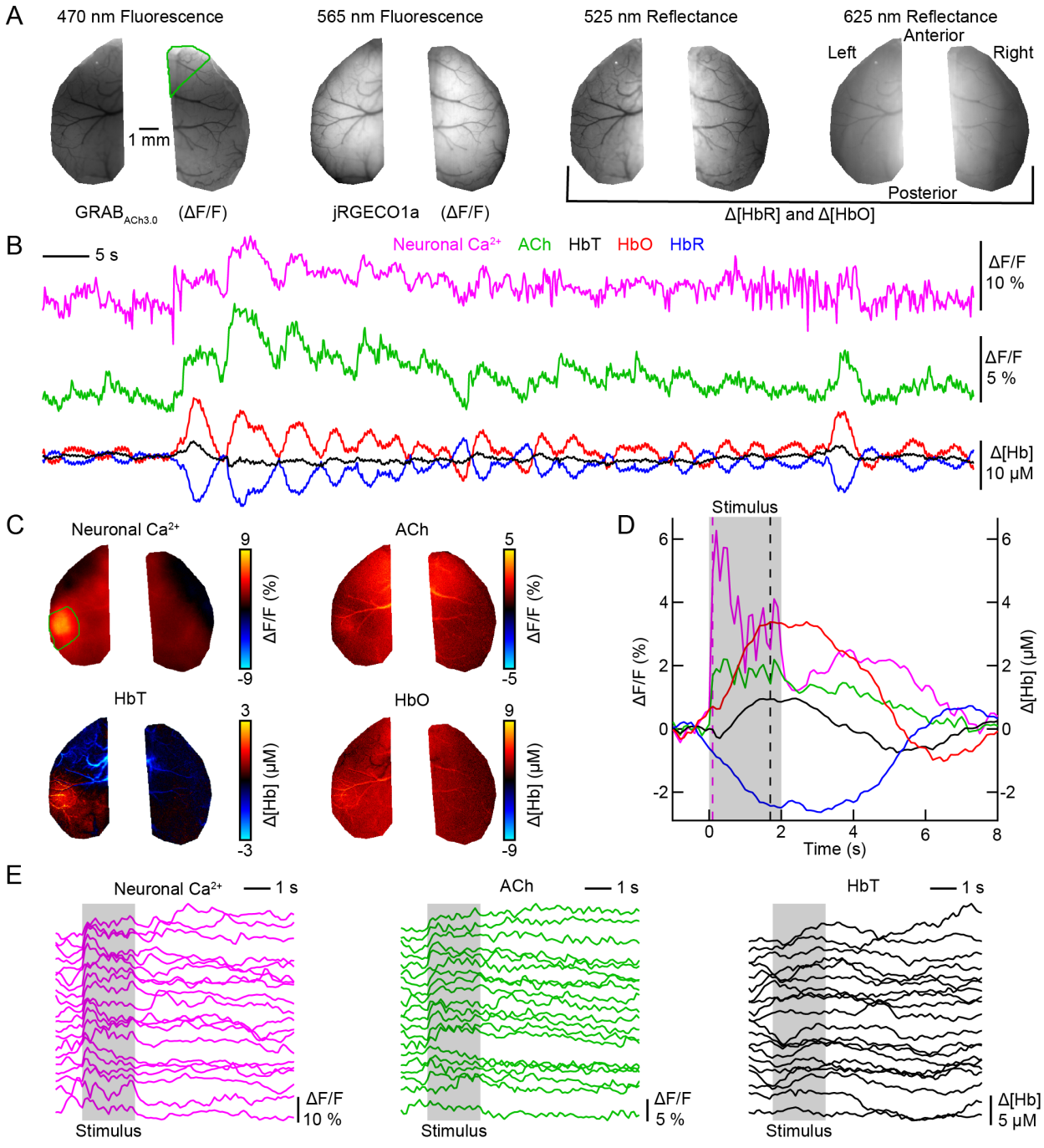
A
470 nm Fluorescence
565 nm Fluorescence
525 nm Reflectance
625 nm Reflectance
Anterior
Left
Right
Posterior
1 mm
GRAB$_{ACh3.0}$ (ΔF/F)
jRGECO1a (ΔF/F)
Δ[HbR] and Δ[HbO]
B
5 s
Neuronal Ca^{2+} ACh HbT HbO HbR
ΔF/F 10 %
ΔF/F 5 %
Δ[Hb] 10 μM
C
Neuronal Ca^{2+}
ACh
HbT
HbO
ΔF/F (%)
Δ[Hb] (μM)
D
Stimulus
ΔF/F (%)
Δ[Hb] (μM)
Time (s)
E
Neuronal Ca^{2+}
ACh
HbT
1 s
Stimulus
ΔF/F 10 %
ΔF/F 5 %
Δ[Hb] 5 μM

Figure 4

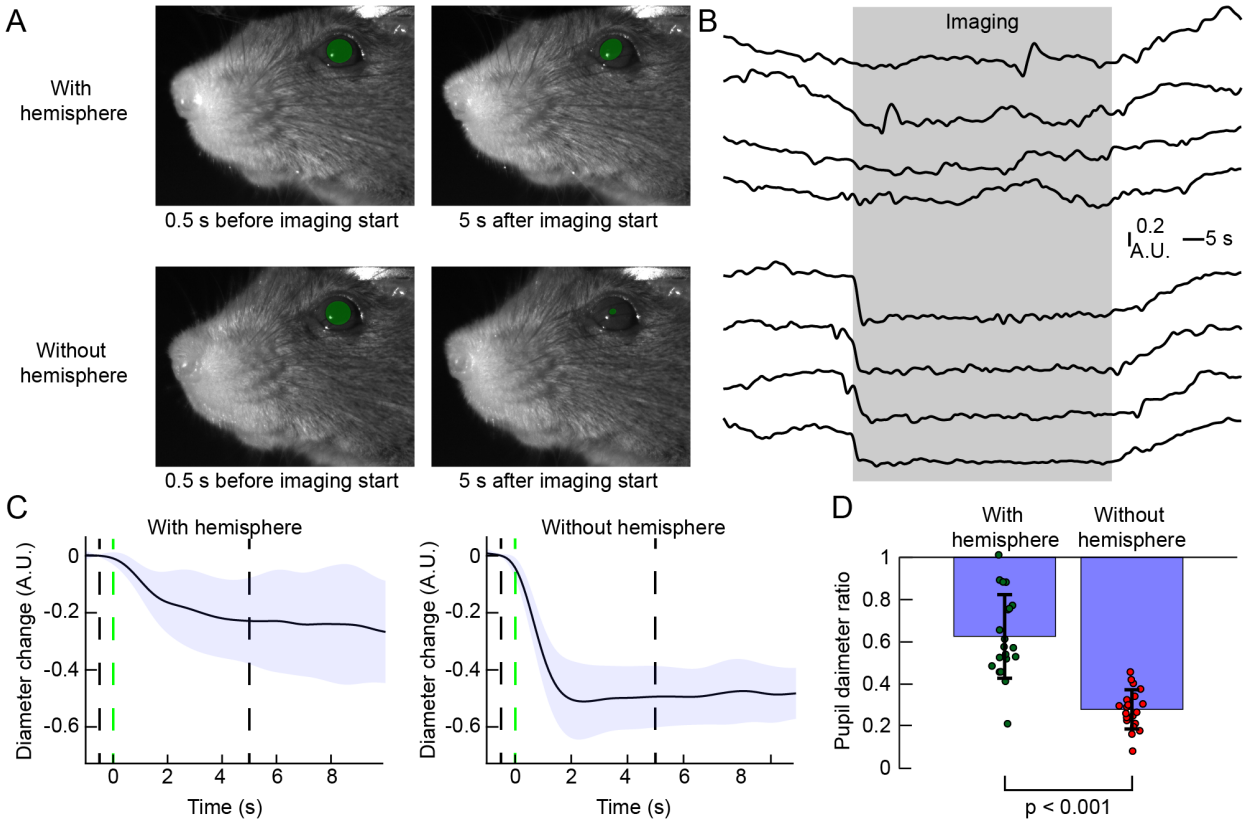
A
With hemisphere
0.5 s before imaging start
5 s after imaging start
Without hemisphere
0.5 s before imaging start
5 s after imaging start
B
Imaging
0.2
A.U.
5 s
C
With hemisphere
Without hemisphere
Diameter change (A.U.)
Time (s)
D
With hemisphere
Without hemisphere
Pupil daimeter ratio
p < 0.001